

Metal–Organic Framework Derived Copper Chalcogenides–Carbon Composites as High-Rate and Stable Storage Materials for Na Ions

Huihua Li, Huang Zhang, Mainer Zarrabeitia, Hai-Peng Liang, Dorin Geiger, Ute Kaiser, Alberto Varzi,* and Stefano Passerini*

Transition metal chalcogenides have been regarded as promising storage materials for sodium ions owing to their high theoretical capacity. Herein, copper-based metal–organic frameworks (Cu-BTC) are reported as precursors to fabricate copper chalcogenides–carbon composites, namely $\text{Cu}_{1.8}\text{S@C}$ and $\text{Cu}_{2-x}\text{Se@C}$. The materials exhibit excellent electrochemical performance with high specific capacities (504 mAh g^{-1} for $\text{Cu}_{1.8}\text{S@C}$ and 317 mAh g^{-1} for $\text{Cu}_{2-x}\text{Se@C}$ at 0.1 A g^{-1}) and long-term cycling stability when used as anode materials in cells employing carbon-coated $\text{Na}_3\text{V}_2(\text{PO}_4)_3$ (NVP/C) positive electrodes. The $\text{Cu}_{2-x}\text{Se@C}||\text{NVP/C}$ cell delivers a specific capacity of 73 mAh g^{-1} at 1.2 A g^{-1} (based on cathode mass) and excellent cycling stability (capacity retention of 85% after 500 cycles at 0.12 A g^{-1}) with Coulombic efficiency of $\approx 99.9\%$. Moreover, the $\text{Cu}_{2-x}\text{Se@C}$ composite performs well as positive electrode storage material in a sodium-metal cell, offering a high reversible capacity of 216 mAh (per gram of $\text{Cu}_{2-x}\text{Se@C}$) after 1800 cycles at 2 A g^{-1} and enabling high specific energy and power.

storage applications and light-duty electromobility to decrease the dependence on the limited lithium (and other metals') resources.^[3,4] SIBs are based on a similar working mechanism as LIBs, nevertheless, challenges pertaining to the electrode materials remain in terms of specific capacity, rate performance, and cycling stability. In this context, the development of suitable electrode materials with reliable cycling performance and high reversible capacity is necessary.

Up to now, several classes of compounds have been investigated as anode and cathode materials for SIBs, such as NASICON-type materials,^[5–7] carbon-based materials,^[8] alloying-type materials,^[9] layered oxides,^[10,11] transition-metal chalcogenides (TMCs),^[12] and others. Among them, TMCs are prospective candidates due to their high theoretical

1. Introduction

Lithium-ion batteries (LIBs) are currently powering devices ranging from portable electronics to electric vehicles.^[1,2] However, to meet the growing demand for efficient low-cost energy storage devices, sodium-ion batteries (SIBs) have been regarded as an alternative technology, especially for large-scale stationary


capacity, easy preparation, and flexible structure design. In particular, Cu-based chalcogenides have attracted interest because of their high reversible specific capacity and electronic conductivity. However, their practical performance is still not satisfactory, hindered by the slow conversion rates and structural variation during sodiation–desodiation process.^[13,14] To address these issues, many strategies have been employed including, e.g., the incorporation of conductive carbon and/or nanostructure engineering. In this respect, integrating nanostructured active material particles into a carbon framework can effectively alleviate volume expansions and further enhance the conductivity of the composite electrode. For example, Fang et al. developed bullet-like $\text{Cu}_9\text{S}_5@N$ -doped carbon hollow particles for SIBs, which exhibited excellent capacity retention of 79% after 4000 cycles at 2 A g^{-1} .^[15] Compared to sulfides, selenides can even provide faster redox kinetics due to more facile bond cleavage.^[16] For example, hierarchical self-decorated Cu_{2-x}Se nanosheets delivered a discharge capacity of nearly 400 mAh g^{-1} at 50 mA g^{-1} in LIBs.^[17] When used as an anode for sodium storage, the nanosheets-assembled CuSe compounds deliver stable capacity even at high rate.^[16]

Metal–organic frameworks (MOFs) have been used as effective self-templates to synthesize functional materials with novel micro-/nano-structures and conductive carbon frameworks for applications in catalysis, gas separation, sensors, and energy storage.^[18–21] In the porous frameworks, the confined metal

H. Li, H. Zhang, M. Zarrabeitia, H.-P. Liang, A. Varzi, S. Passerini
 Helmholtz Institute Ulm (HIU)
 Helmholtzstrasse 11, D-89081 Ulm, Germany

H. Li, H. Zhang, M. Zarrabeitia, H.-P. Liang, A. Varzi, S. Passerini
 Karlsruhe Institute of Technology (KIT)
 P.O. Box 3640, D-76021 Karlsruhe, Germany
 E-mail: alberto.varzi@kit.edu; stefano.passerini@kit.edu

D. Geiger, U. Kaiser
 Central Facility for Electron Microscopy
 Group of Electron Microscopy of Materials Science
 Ulm University
 Albert-Einstein-Allee 11, 89081 Ulm, Germany

 The ORCID identification number(s) for the author(s) of this article can be found under <https://doi.org/10.1002/adsu.202200109>.

© 2022 The Authors. Advanced Sustainable Systems published by Wiley-VCH GmbH. This is an open access article under the terms of the Creative Commons Attribution License, which permits use, distribution and reproduction in any medium, provided the original work is properly cited.

DOI: 10.1002/adsu.202200109

species can be easily transformed into metal oxides,^[22] phosphides,^[23] selenides,^[24] and sulfides^[14] during the pyrolysis process. Besides, the organic ligands can be carbonized and turned into a conductive framework acting as host matrix for the above-mentioned particles. This effectively enhances the electronic conductivity and prevents the materials aggregation and structural variation upon sodiation–desodiation. These features are particularly appealing to fabricate high-performance composite electrode materials for batteries. Benefiting from the abundant copper (Cu), the Cu-based metal-organic frameworks (Cu-BTC) (also known as HKUST-1), composed of benzene-1,3,5-tricarboxylate (BTC) linkers and binuclear copper paddlewheel units, has been widely investigated in electrode material fabrication for energy storage systems, such as supercapacitors and LIBs.^[25,26] For example, the synthesis of copper sulfide (Cu_xS) composites by the temperature-controlled sulfuration of a prototypal Cu metal-organic framework (MOF) was reported.^[27] These materials exhibited high reversible capacity as anodes for LIBs. Similarly, Cu_xS @Cu-BTC composite materials were also fabricated and studied as anode materials for LIBs, exhibiting an excellent electrochemical performance.^[25] Recently, Xiao et al. designed and synthesized Cu_{1.8}Se@C-500 °C by Cu-BTC-derived in situ carbon-encapsulation strategy. The materials show excellent performance as anode material for Li-ion batteries with a specific capacity of 416 mA h g⁻¹ after 500 cycles at 1 A g⁻¹.^[28] These results demonstrate the feasibility of using Cu-based MOFs derived sulfidation/selenidation strategy to synthesize in situ carbon-encapsulated sulfides/selenides as superior electrode materials for SIBs.

Herein, we report two Cu-based chalcogenides embedded in carbonaceous frameworks, i.e., Cu_{1.8}S@C and Cu_{2-x}Se@C, fabricated by MOF-derived sulfidation and selenidation, respectively. The systematical investigation of their morphological, structural, and electrochemical properties as versatile Na-ion storage materials is reported. The MOF-derived Cu_{1.8}S@C and Cu_{2-x}Se@C demonstrate outstanding electrochemical performance with long cycling stability, superior rate capability, and high reversible capacities. Cells featuring carbon-coated Na₃V₂(PO₄)₃ (NVP/C) cathodes were fabricated, showing promising reversible capacity and long-term cycling stability. Besides the general application as anodes, we also investigated the performance as potential positive electrode materials for SMBs, where the Na||Cu_{2-x}Se@C and Na||Cu_{1.8}S@C cells also deliver high energy and power densities. The reaction mechanism and corresponding structural evolution during Na⁺ insertion and extraction were studied by in situ X-ray diffraction (XRD), evidencing higher reversibility of the conversion reaction for Cu_{2-x}Se@C.

2. Results and Discussion

2.1. Material Synthesis and Characterization

The crystal structures of the Cu-BTC derived samples were identified by powder XRD. The XRD pattern of Cu_{2-x}Se@C composite is presented in **Figure 1**. The reflections can be assigned to the berzelianite Cu_{2-x}Se in cubic phase structure (JCPDS NO. 06-0680), with the three sharp peaks at 26.7, 44.6, and 52.9° reflecting the (111), (220), and (311) planes, respectively. The carbon framework in Cu_{2-x}Se@C was investigated

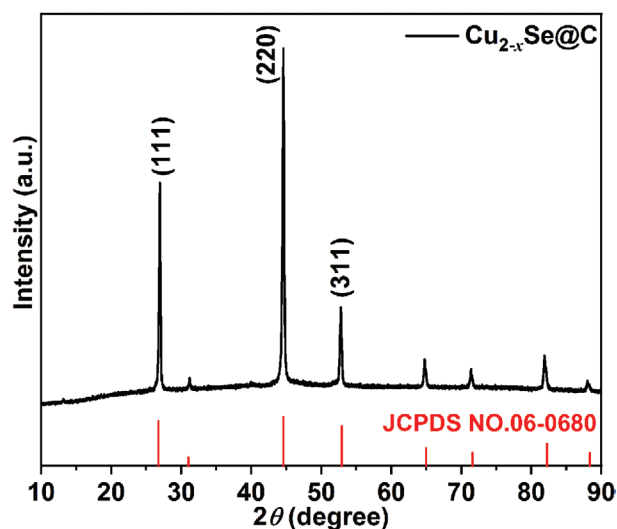


Figure 1. XRD patterns of Cu_{2-x}Se@C.

by Raman spectroscopy (Figure S1a, Supporting Information). The characteristic peaks at around 1370 and 1578 cm⁻¹ can be assigned to the D-band (disordered sp³-type carbon) and G-band (the graphitic sp²-type carbon), respectively. Noticeably, the intensity of G-band is higher than D-band, indicating a relatively high content of graphitic (sp²-hybridized) carbon. The XRD and Raman spectroscopy investigation of Cu_{1.8}S@C has been shown in Figure S1b,c (Supporting Information), and the results are in good agreement with the literature.^[27,29] The XRD patterns reveals that Cu_{1.8}S@C also owns the cubic crystalline structure, however, Cu_{2-x}Se@C has higher crystallinity. The Raman spectrum shows that the D/G-band (I_D/I_G) ratio for Cu_{1.8}S@C is 1.0, i.e., higher than the one for Cu_{2-x}Se@C (0.92). This suggests that the fraction of disordered (sp³-type) carbon in Cu_{1.8}S@C is higher than in Cu_{2-x}Se@C. The porosity of the Cu_{1.8}S@C and Cu_{2-x}Se@C was examined with gas absorption and desorption measurements in Ar (87 K). The isotherms and pore size distribution are displayed in Figure S2 (Supporting Information). The BET results reveal the specific surface areas of Cu_{1.8}S@C and Cu_{2-x}Se@C being 24.7 and 58.5 m² g⁻¹, respectively. The type II isotherm with a slight slope in the medium-high relative pressures, and pore size distribution results, evidence a mostly micro-mesoporous character of both Cu_{1.8}S@C and Cu_{2-x}Se@C.

The surface chemical composition of Cu_{1.8}S@C and Cu_{2-x}Se@C was characterized by X-ray photoelectron spectroscopy (XPS). The high-resolution Cu 2p_{3/2} spectra are displayed in **Figure 2a,b** for Cu_{1.8}S@C and Cu_{2-x}Se@C, respectively. The main peak is located at 932.1 eV in both samples, which can be ascribed to Cu⁺.^[30] In order to identify the Cu⁺ species in each material, the copper Auger parameter is calculated (the sum of binding energy of the main Cu 2p peak and the Cu LMM kinetic energy). This methodology is well-known to be more accurate for identifying compounds and it is commonly used for transition-metal species.^[31] The calculated Auger parameter of Cu_{1.8}S@C is 1850.0 eV, which is in line with Cu_{1.8}S (note that the Auger parameter of Cu₂S and CuS is 1849.8 and 1850.3 eV, respectively).^[32] On the other hand, the calculated Auger parameter of Cu_{2-x}Se@C is 1850.1 eV, i.e., it is slightly higher than

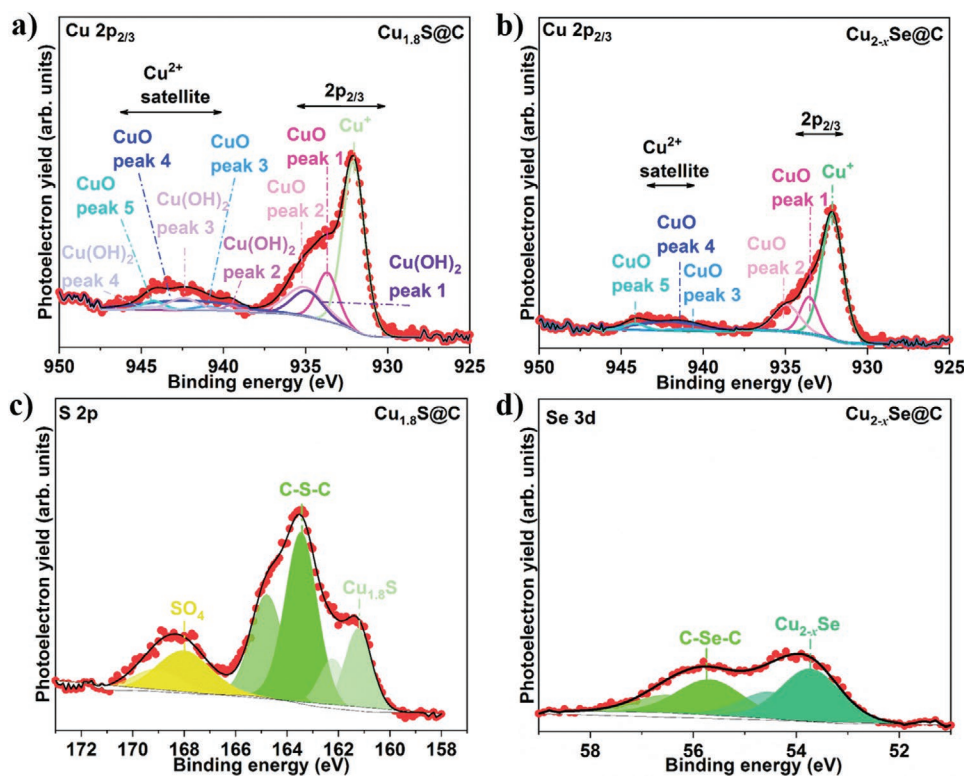


Figure 2. High-resolution XPS spectra of a,b) Cu 2p for $\text{Cu}_{1.8}\text{S}@C$ and $\text{Cu}_{2-x}\text{Se}@C$, respectively. c) S 2p for $\text{Cu}_{1.8}\text{S}@C$ and d) Se 3d for $\text{Cu}_{2-x}\text{Se}@C$.

Cu_2Se (1849.9 eV) and lower than CuSe (1850.4 eV), suggesting that the surface composition ranges between $x = 0$ and 1, in line with the XRD results.^[32] Moreover, the lower intensity peaks in $\text{Cu}_{1.8}\text{S}@C$ and $\text{Cu}_{2-x}\text{Se}@C$ can be ascribed to Cu^{2+} and its satellite peaks,^[33] which are characteristics of Cu^{2+} due to its paramagnetic behavior.^[30,34] It should be noted that CuS and CuSe do not exhibit shake-up peaks because Cu^{2+} in these species is weakly paramagnetic. In contrast, CuO or $\text{Cu}(\text{OH})_2$ show high paramagnetic behavior, suggesting the presence of oxides and/or hydroxides on the surface of $\text{Cu}_{1.8}\text{S}@C$ and $\text{Cu}_{2-x}\text{Se}@C$. The $\text{Cu}2p_{3/2}$ region suggested that the Cu^{2+} species in $\text{Cu}_{1.8}\text{S}@C$ correspond to CuO and $\text{Cu}(\text{OH})_2$, showing five and four peaks for each species, respectively.^[30] The first peak of CuO appears at 933.6 eV and the following peaks toward higher binding energies of 1.37, 741, 8.54, and 10.59 eV with respect to the first peak. Meanwhile the peaks at 934.9, 939.5, 942.4, and 944.3 eV corresponds to $\text{Cu}(\text{OH})_2$.^[30] In the case of $\text{Cu}_{2-x}\text{Se}@C$ five peaks are observed at 933.5, 934.9, 940.9, 942.1, and 944.1 eV, which correspond to $\text{Cu}(\text{II})\text{O}$. The O 1s spectra are also analyzed to correlate the possible oxides and hydroxides formation on the surface of $\text{Cu}_{1.8}\text{S}@C$ and $\text{Cu}_{2-x}\text{Se}@C$ (see Figure S3a,b, Supporting Information). On the one hand, the O 1s spectrum of $\text{Cu}_{1.8}\text{S}@C$ exhibits the presence of $\text{O}_a\text{-C}=\text{O}_b$ (531.5 and 533.8 eV for O_a and O_b , respectively), $-\text{CO}-$ (532.7 eV, may contain some SO_x traces in line with S 2p photoelectron shown below), $\text{Cu}(\text{OH})_2$ (531.4 eV), and $\text{Cu}(\text{II})\text{O}$ (530.7 eV). On the other hand, $\text{Cu}_{2-x}\text{Se}@C$ exhibits the same peaks ($\text{O}_a\text{-C}=\text{O}_b$, at 531.4 and 533.8 eV, $-\text{CO}-$ at 532.7 eV and $\text{Cu}(\text{II})\text{O}$ at 530.5 eV), expected for $\text{Cu}(\text{OH})_2$, in agreement with Cu 2p_{3/2} region.^[30] These results suggested that in the case of

$\text{Cu}_{1.8}\text{S}@C$ both hydroxides and oxides are formed, while in the $\text{Cu}_{2-x}\text{Se}@C$ mainly oxides are present on the surface. Additionally, the S 2p spectrum of $\text{Cu}_{1.8}\text{S}@C$ is presented in Figure 2c. As shown, there are three main S species in the materials.^[35] The peaks at 161.2/162.2 eV (S 2p_{2/3} and S 2p_{1/2}, respectively) can be assigned to sulfide (S^{2-}) species in the nonstoichiometric $\text{Cu}_{1.8}\text{S}@C$.^[14] The main doublet at 163.4/164.8 eV can be attributed to S atoms in the carbonaceous framework (C-S-C),^[36] while the peak at higher binding energies (168.1/169.1 eV) to oxidized S species, for example SO_4 , $\text{SO}_x\text{-C}$, etc.^[8] In the $\text{Cu}_{2-x}\text{Se}@C$ sample (Figure 2d), the Se 3d spectrum shows two main Se-based species, among which the first one at 53.7/54.6 eV (Se 3d_{5/2} and Se 3d_{3/2} respectively) corresponding to the metal selenide, which appears at slightly lower binding energy than the pure Cu_2Se ,^[33,37] indicating that the copper selenide is in nonstoichiometric state, in line with the Auger parameter value. The other peak at 55.7/56.5 eV is related to C-Se-C bonds, suggesting that Se is also chemically doped into the carbon.^[38,39] Finally, the C 1s spectra of $\text{Cu}_{1.8}\text{S}@C$ and $\text{Cu}_{2-x}\text{Se}@C$ is analyzed (see Figure S3c,d, Supporting Information). In both samples four obvious peaks can be detected at 284.4, 285.0, 286.0, and 288.6 eV, which are related to the $-\text{C}=\text{C}(\text{sp}^2\text{ carbon})$, $-\text{C}-\text{C}/-\text{C}-\text{H}$ (hydrocarbons), $-\text{CO}-$ (ethers), and $-\text{COOR}$ (esters) groups, respectively.^[37] These results confirm that carbon-encapsulated $\text{Cu}_{1.8}\text{S}@C$ and $\text{Cu}_{2-x}\text{Se}@C$ composites have been successfully synthesized via the one-step sulfidation/selenidation of Cu-BTC. In addition, the mass content of copper sulfide and copper selenide in the $\text{Cu}_{1.8}\text{S}@C$ and $\text{Cu}_{2-x}\text{Se}@C$ was also determined using thermogravimetric analysis (TGA) measurements in O_2 (Figure S4, Supporting

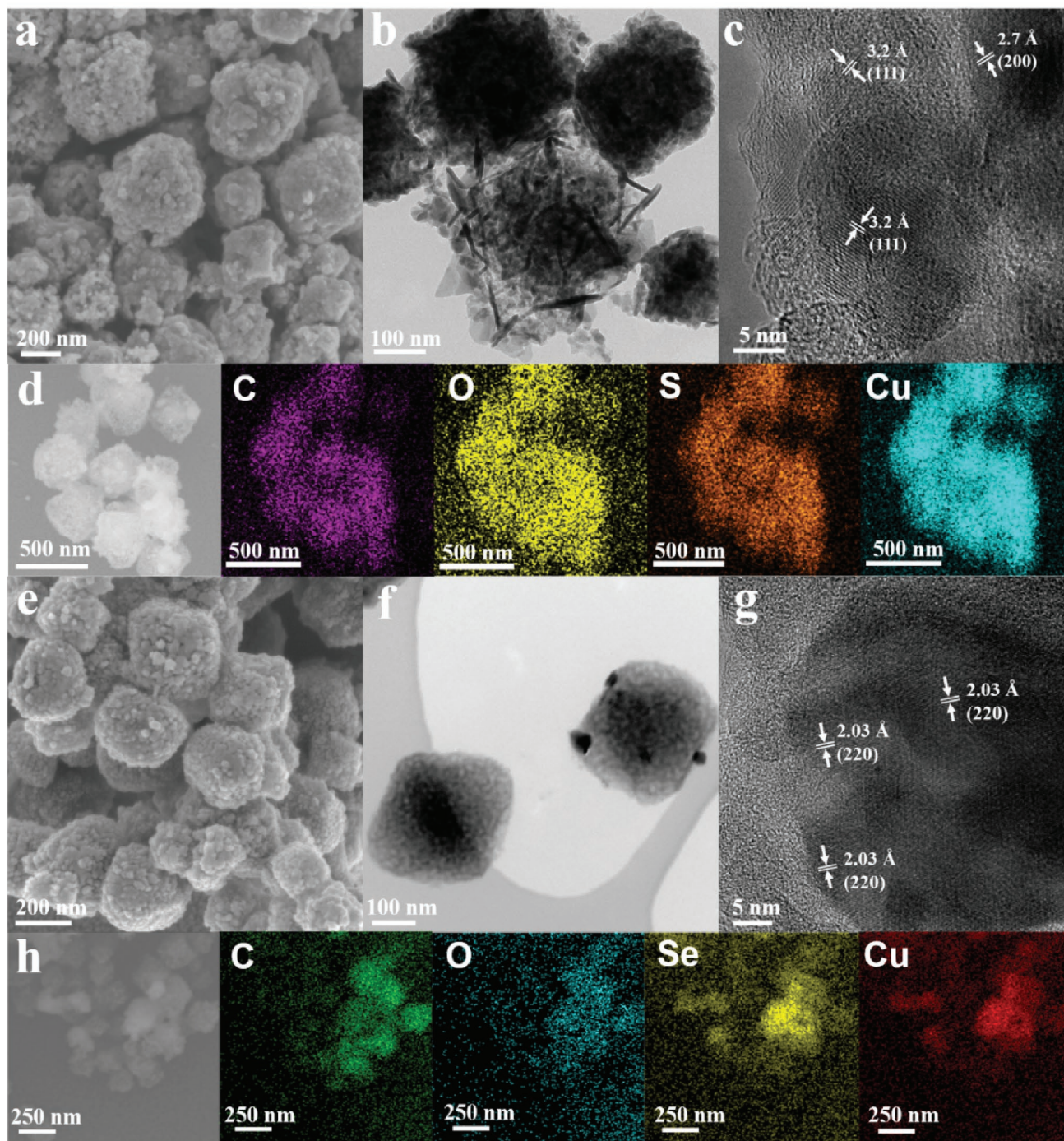


Figure 3. Morphological and structural features of $\text{Cu}_{1.8}\text{S}@C$ and $\text{Cu}_{2-x}\text{Se}@C$. a) SEM, b,c) HR-TEM, and d) Elemental mapping images of $\text{Cu}_{1.8}\text{S}@C$. e) SEM, f,g) HR-TEM, and h) Elemental mapping images of $\text{Cu}_{2-x}\text{Se}@C$.

Information). Assuming that the $\text{Cu}_{1.8}\text{S}@C$ and $\text{Cu}_{2-x}\text{Se}@C$ composites were fully transformed into CuO during the heating process under O_2 atmosphere, the content of copper sulfide and copper selenide in the composites was calculated to be 67 wt.% and 78 wt.%, respectively. The detailed calculations can be found in the Supporting Information.

The morphology and microstructure of $\text{Cu}_{1.8}\text{S}@C$, and $\text{Cu}_{2-x}\text{Se}@C$ composites were investigated by scanning electron

microscopy (SEM) and transmission electron microscopy (TEM). The overall morphology is well maintained after sulfidation/selenidation, as shown in shown in **Figure 3a,b,e,f**. However, the surface of the $\text{Cu}_{1.8}\text{S}@C$ and $\text{Cu}_{2-x}\text{Se}@C$ becomes uneven and rough, due to the decomposition of the organic ligands and growth of the metal selenide particles. The TEM images distinctly demonstrate that the $\text{Cu}_{1.8}\text{S}$ and Cu_{2-x}Se particles are encapsulated in the carbon matrix, as previously

suggested by XPS. The high-resolution TEM images display the lattice fringes of (111) and (200) planes for $\text{Cu}_{1.8}\text{S}$ with d -spacing of 3.2 and 2.7 Å, respectively, and the lattice fringes of the (220) plane of Cu_{2-x}Se with the d -spacing of 2.03 Å (Figure 3c,g). The elemental mapping results of $\text{Cu}_{1.8}\text{S}@C$ and $\text{Cu}_{2-x}\text{Se}@C$ (Figure 3d,h) indicate that Cu, O, S, or Se atoms are homogeneously distributed in the carbonaceous frameworks.

2.2. Electrochemical Performance

2.2.1. Sodium Storage Mechanism and Performance of $\text{Cu}_{2-x}\text{Se}@C$

$\text{Cu}_{2-x}\text{Se}@C$ composite was evaluated as sodium storage material in the potential window from 0.01 to 2.5 V (vs Na^+/Na) using ether-based electrolyte (1 M NaPF_6 in diethylene glycol dimethyl ether (DEGDME)). Figure 4a shows the CVs of a $\text{Cu}_{2-x}\text{Se}@C$ electrode recorded at a scan rate of 0.1 mV s^{-1} . Upon the first cathodic scan, two intensive peaks at 1.94 and 1.63 V were detected, which may be related to the intercalation of Na^+ into the Cu_{2-x}Se . A very broad cathodic peak at 0.94 V corresponds to the subsequent reduction into Na_2Se and Cu^0 and, most likely, to the electrolyte decomposition and solid electrolyte interphase (SEI) formation.^[8,40] The small cathodic peak at 0.05 and anodic peak at 0.07 V can be assigned to the reversible Na storage in the conductive carbon matrix and

carbon additive.^[14,29] During the first anodic scan, two main peaks are present at 1.53 and 2.04 V, representing the stepwise conversion reaction between Na_2Se and Cu^0 to form NaCuSe and Cu_{2-x}Se , respectively. From the second cycle onwards, all curves exhibit good reproducibility, indicating the high reversibility of the process. Figure 4b shows the galvanostatic charge–discharge (GCD) profiles of the $\text{Cu}_{2-x}\text{Se}@C$ electrode at 0.2 A g^{-1} , where all the voltage plateaus are consistent with the CV results. The initial sodiation and desodiation capacities are 473 and 319 mAh g^{-1} with an initial Coulombic efficiency (CE) of 67.4%. After 70 cycles, the capacity delivered is 310 mAh g^{-1} , corresponding to a capacity retention of 97.3% (Figure S5a, Supporting Information). To verify the mechanical integrity of the $\text{Cu}_{2-x}\text{Se}@C$ composite after the charge–discharge processes, the morphology of the electrode after 70 cycles at 0.2 A g^{-1} was investigated by SEM (Figure S5b, Supporting Information). The micrograph shows that the $\text{Cu}_{2-x}\text{Se}@C$ particles retain their original structure, and buffer well the volume strain upon repeated (de)sodiation reactions. The rate performance of the $\text{Cu}_{2-x}\text{Se}@C$ electrode was also evaluated, as shown in Figure 4c and Figure S5c, Supporting Information. The material displays reversible capacities of 317, 313, 303, 295, 286, 272, and 257 mAh g^{-1} at 0.1, 0.2, 0.5, 1, 2, 5, and 10 A g^{-1} , respectively. Figure S5c, Supporting Information, shows the corresponding (dis)charge profiles of $\text{Cu}_{2-x}\text{Se}@C$ from 0.1 to 10 A g^{-1} . All profiles exhibit very small polarization

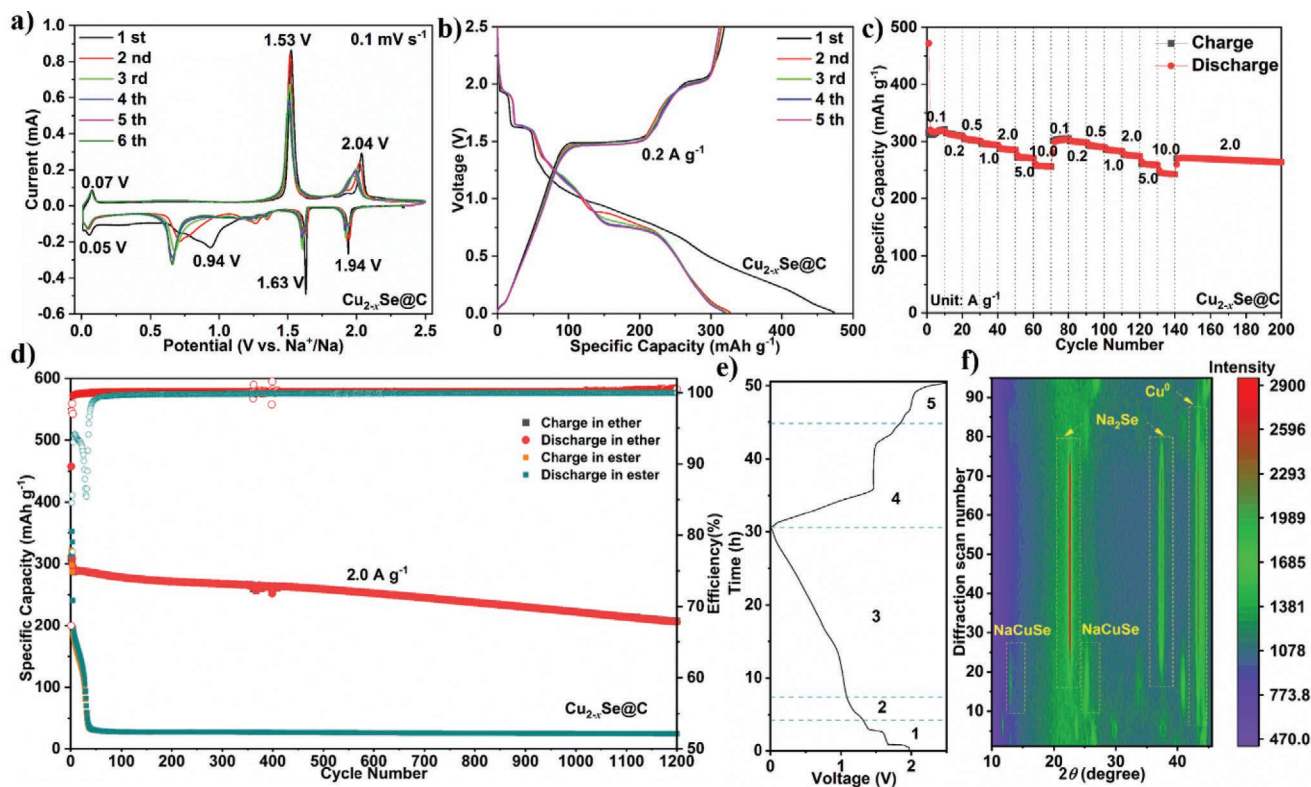


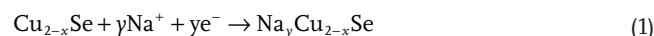
Figure 4. Sodium storage performance and mechanism of $\text{Cu}_{2-x}\text{Se}@C$ in the potential range of 0.01–2.5 V. a) CV curves at a scan rate of 0.1 mV s^{-1} . b) Galvanostatic charge–discharge curves of the initial five cycles at 0.2 A g^{-1} . c) Rate capability at various current densities, ranging from 0.1 to 10 A g^{-1} . d) Long-term cyclic performance at the current density of 2 A g^{-1} for 1200 cycles in ether and ester-based electrolytes (after 3 cycles at 0.1 A g^{-1} in the beginning as activation step). In situ measurements of the $\text{Cu}_{2-x}\text{Se}@C$ electrode. e) Discharge–charge profile. f) In situ XRD patterns in a contour plot recorded consecutively during (dis-)charge (scans 1–95).

between the charge and discharge voltage plateaus, reflecting fast electrode kinetics. In addition, the long-term cycling performance of $\text{Cu}_{2-x}\text{Se}@C$ was also evaluated in ether and ester-based electrolytes as shown in Figure 4d. After 1200 cycles at 2 A g^{-1} , the electrode in ether-based electrolyte retains 88.1% of the capacity with respect to the fourth cycle (excluding the initial 3 cycles at 0.1 A g^{-1} as activation step). However, it is found that the electrode in ester-based electrolyte displays an obvious capacity decay from the initial cycles. In comparison to previous studies on copper selenide and other transition metal selenide-based composites, this MOF-derived composite material shows superior sodium storage performance, especially at high current densities (Table S1, Supporting Information). For comparison, the electrochemical performance of $\text{Cu}_{1.8}\text{S}@C$ was also evaluated in the same potential window from 0.01 to 2.5 V using the same electrolyte as presented in Figures S6 and S7, and Table S2 (see the Supporting Information for a detailed discussion of $\text{Cu}_{1.8}\text{S}@C$ anode). Specifically, $\text{Cu}_{1.8}\text{S}@C$ also displays excellent sodium storage of 492 mA h g^{-1} at 0.1 A g^{-1} after 200 cycles in DEGDME electrolyte, together with a good rate capability and an improved long cycling stability at 2 A g^{-1} .

In situ XRD analysis was employed to investigate the sodium storage mechanism and structural evolution of $\text{Cu}_{2-x}\text{Se}@C$ upon the first (de)sodiation process. The simultaneously recorded GCD voltage profiles and XRD patterns (95 scans) are shown in Figure 4e,f. As displayed in Figure 4f, $\text{Cu}_{2-x}\text{Se}@C$ experiences multiple reactions during the (de)sodiation process. Specifically, from OCV to 1.32 V (region 1, scans 1–8), four additional peaks gradually appear at 11.9 , 23.7 , 29.9 , and 37.5° (Figure 4f and Figure S8a, Supporting Information), which can be assigned to the Na^+ intercalated $\text{Na}_y\text{Cu}_{2-x}\text{Se}$ phase (Equation 1). In region 2 (from 1.32 to 1.08 V, scans 9–14), a series of new peaks associated to NaCuSe (13.0 , 25.3 , 33.6 , and 40.8° , JCPD No. 31–0480) can be detected (Figure 4f and Figure S8b, Supporting Information), as a result of the continuous uptake of Na^+ (Equation 2). Upon deep sodiation (region 3, from 1.08 to 0.01 V, scans 15–58), the signals of Na_2Se (22.6 and 37.2° , JCPDS No. 23–0527) gradually evolve along with the Cu^0 diffraction peaks and the disappearance of the features characteristic of NaCuSe (Figure 4f and Figure S8c, Supporting Information), demonstrating a conversion reaction resulting in the formation of Na_2Se and metallic copper (Equation 3). At the end, the sodiation–desodiation reactions of carbon should occur at low potential (Equations 4 and 5). Unfortunately, similarly to the case of $\text{Cu}_{1.8}\text{S}@C$, the carbon structural evolution could not be observed via in situ XRD. During the following desodiation process (region 4, from 0.01 to 1.98 V, scans 59–88), the intensities of Na_2Se and Cu^0 peaks gradually decrease, accompanied by the re-appearance of NaCuSe (Figure 4f and Figure S8d, Supporting Information). This is due to the conversion of Na_2Se and Cu^0 back to the NaCuSe (Equation 6). When charging up to 2.5 V (region 5, from 1.98 to 2.5 V, scans 89–95), the peaks of NaCuSe completely vanished and the signals of Cu_{2-x}Se gradually increased again (Figure 4f and Figure S8e, Supporting Information), suggesting the reversible transformation from NaCuSe to Cu_{2-x}Se (Equation 7). The in situ XRD measurement was also adopted to investigate the electrochemical reaction mechanism of $\text{Cu}_{1.8}\text{S}@C$ upon the first (de)sodiation process (Figures S9 and S10, Supporting Information). A

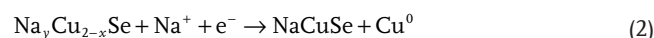
detailed description is provided in the Supporting Information. Interestingly, contrary to what has been observed in the case of the sulfide, only the peaks of Cu_{2-x}Se could be observed at full charge of $\text{Cu}_{2-x}\text{Se}@C$ (no residual Na_2Se), demonstrating that the conversion reaction of selenides is more reversible. In summary, the sodiation and desodiation process in $\text{Cu}_{2-x}\text{Se}@C$ could be described by the following equations:

Discharge: Region 1



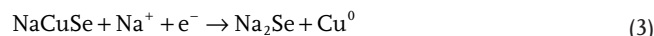
(OCV–1.32 V, Insertion)

Region 2



(1.32–1.08 V, Conversion, reaction not balanced)

Region 3



(1.08–0.01 V, Conversion)

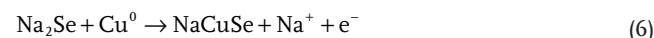


(Below 0.5 V, Insertion in Carbon)

Charge: Region 4

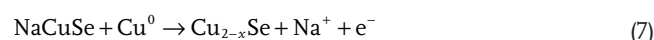


(Above 0.01 V, De-insertion from Carbon))



(0.01–1.98 V, Conversion)

Region 5



(1.98–2.5 V, De-insertion, reaction not balanced)

2.2.2. Electrochemical Performance of $\text{Cu}_{2-x}\text{Se}@C||\text{NVP}/C$ and $\text{Na}||\text{Cu}_{2-x}\text{Se}@C$ Cells and Their Comparison

Inspired by the excellent electrochemical storage performance of $\text{Cu}_{2-x}\text{Se}@C$, the electrodes based on this composite material were studied in full cells, both as the negative and the positive electrode. First, $\text{Cu}_{2-x}\text{Se}@C||\text{NVP}/C$ full cells were fabricated employing a presodiated $\text{Cu}_{2-x}\text{Se}@C$ anode and an NVP/C cathode (Figure 5a). To understand the potential evolution of the single electrodes, a sodium pseudo-reference electrode was also employed. Figure 5b displays the capacity of the cathode upon full utilization, which can be expected by the cathode-limited cell balancing. The $\text{Cu}_{2-x}\text{Se}@C||\text{NVP}/C$ full cell delivers specific capacities of 111, 105, 100, 95, 90, 81 and 73 mAh g^{-1} (based on the cathode active material mass) at 0.1 C, 0.2 C, 0.5 C, 1 C, 2 C, 5 C, and 10 C, respectively, in the voltage range of 0.4–3.6 V (Figure 5c). At 0.1 C and 0.2 C, a capacity

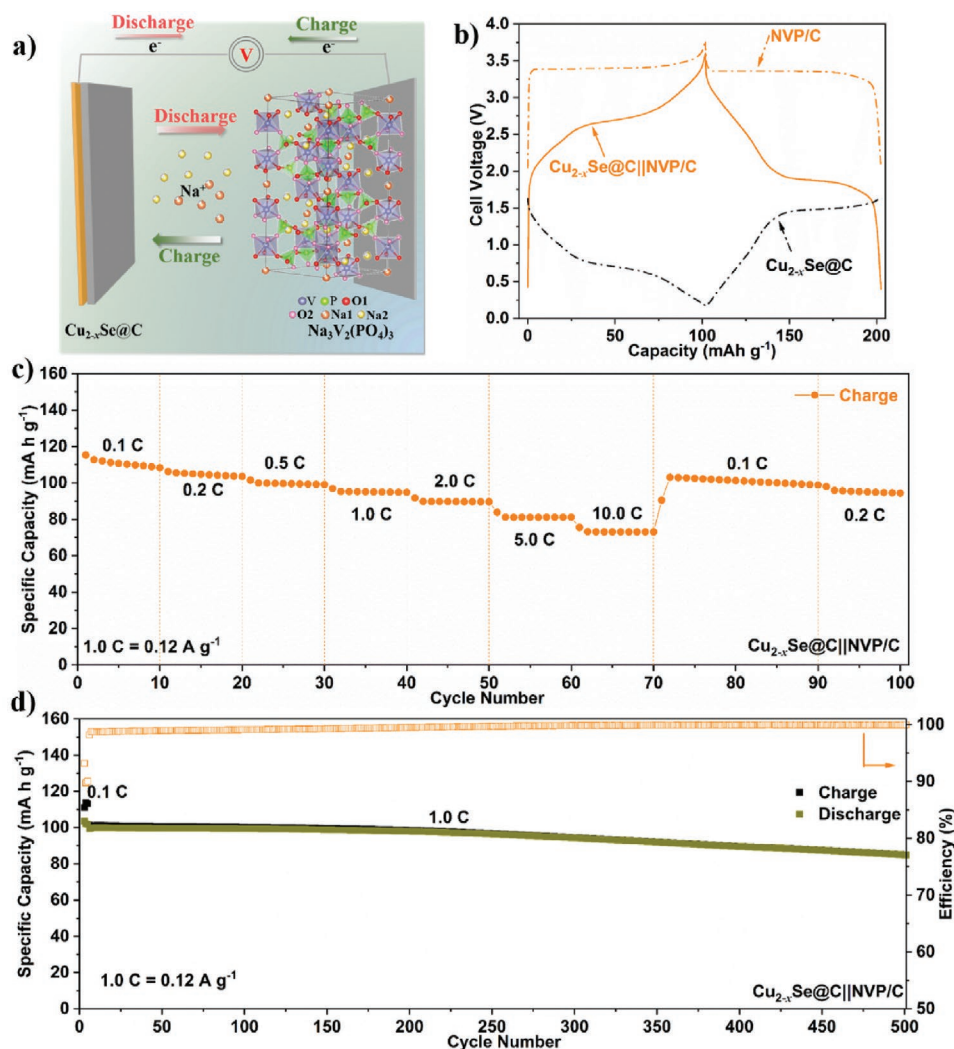


Figure 5. Electrochemical performance of a $\text{Cu}_{2-x}\text{Se}@C||\text{NVP}/C$ full cell within the 0.4–3.6 V voltage window. a) Schematic illustration of $\text{Cu}_{2-x}\text{Se}@C||\text{NVP}/C$ full cells. b) Representative galvanostatic discharge–charge profile of the full cell at 0.12 A g^{-1} (orange solid line) as well as the NVP/C cathode (orange dashed/dotted line) and $\text{Cu}_{2-x}\text{Se}@C$ (black dashed/dotted line) versus the sodium reference. c) Rate capability at various current densities, ranging from 0.1 C to 10 C. d) Long-term cycling performance at 1 C (after 3 cycles at 0.1 C in the beginning as activation step). (1 C = 120 mA g^{-1}).

comparable to the initial values is recovered, demonstrating the high reversibility of $\text{Cu}_{2-x}\text{Se}@C$ as anode. Furthermore, the full cell underwent a long-term cycling test at 1 C (after 3 cycles at 0.1 C as activation step). A specific capacity of 85 mAh g^{-1} (based on the cathode active material) is maintained after 500 cycles, with a high CE of 99.9% (Figure 5d). These results confirm that the $\text{Cu}_{2-x}\text{Se}@C$ can be an efficient anode material for fabricating high performance SIBs.

However, considering the substantial amount of charge delivered at high potentials $\text{Cu}_{2-x}\text{Se}@C$ can also be considered as positive electrode in a sodium-metal cell. In this context, we investigated the electrochemical performance of a $\text{Na}||\text{Cu}_{2-x}\text{Se}@C$ cell by limiting the discharge potential to 0.5 V (the cell was only initially discharged to 0.01 V for one cycle to allow for complete SEI formation). Figure 6a displays the CV curves at a scan rate of 0.1 mV s^{-1} in a three-electrode cell. The first sweep was performed in the potential window of 0.01–3.0 V (vs Na^+/Na). The voltammogram is analogous to

the one obtained between 0.01 and 2.5 V (see Figure 4a). This means that when the lower cut-off potential is limited at 0.5 V, only the Na^+ insertion in the carbon matrix is excluded. As demonstrated in the GCD profiles (Figure 6b), the cell delivers a capacity of 275 mAh g^{-1} when discharged to 0.5 V at 0.1 A g^{-1} , which is only negligibly lower than the one obtained in the full potential range. The cycling stability of $\text{Cu}_{2-x}\text{Se}@C$ as cathode in sodium-metal cell was initially investigated at 0.1 A g^{-1} . The reversible capacity reaches a stable value of 275 mAh g^{-1} after 50 cycles (Figure S11a, Supporting Information). This lower capacity when limiting the discharge to 0.5 V is because the carbon matrix does not act as the sodium host anymore, and only the conversion reaction is “active.” This is further confirmed by in situ XRD (Figure S11b, Supporting Information), in which the discharge cut-off voltage is limited to 0.5 V. The peaks of NaCuSe have completely disappeared, proving the complete conversion reaction at this potential. The rate performance of the $\text{Na}||\text{Cu}_{2-x}\text{Se}@C$ cell was evaluated at various

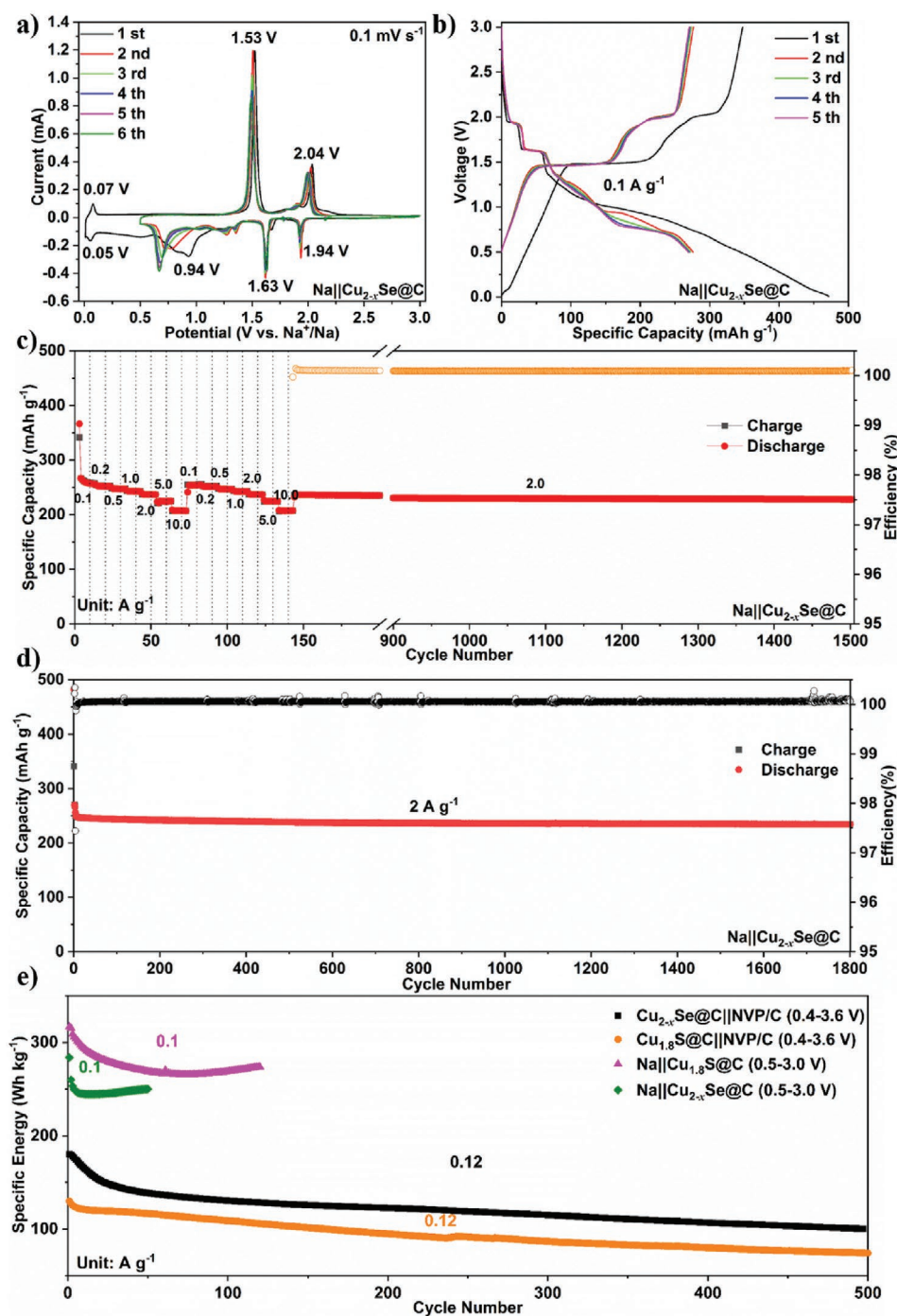


Figure 6. Electrochemical performance of Na||Cu_{2-x}Se@C cell. a) CV curves at a scan rate of 0.1 mV s⁻¹. b) Galvanostatic charge–discharge curves of the initial five cycles at 0.1 A g⁻¹. c) Rate capability at various current densities, ranging from 0.1 to 10 A g⁻¹. d) Long-term cycling performance at the current density of 2 A g⁻¹ for 1800 cycles (after 3 cycles at 0.1 A g⁻¹ in the beginning as activation step). e) Energy density of full-cells. The capacity values in panels (b), (c), and (d) are given with respect to the Cu_{2-x}Se@C weight.

specific currents (Figure 6c and Figure S11c, Supporting Information). The average specific capacities are 260, 253, 248, 243, 237, 224, and 207 mAh g⁻¹ at 0.1, 0.2, 0.5, 1, 2, 5, and 10 A g⁻¹, respectively. Moreover, the long-term cycling stability after the rate performance test was probed under a high current load of 2 A g⁻¹ for more than 1350 cycles. An identical test was also

performed on a fresh Na||Cu_{2-x}Se@C cell, which could reach 1800 cycles (Figure 6d) without any obvious capacity decay.

In the same way, the electrochemical performance of Cu_{1.8}S@C||NVP/C and Na||Cu_{1.8}S@C cells was also investigated. The Cu_{1.8}S@C||NVP/C cell displays a satisfactory cycling stability during the initial 50 cycles at 1.0 C (Figure S12, Supporting

Information). However, a slight capacity decay is observed upon prolonged operation for 500 cycles. On the contrary, the Na||Cu_{1.8}S@C cell displays a superior rate capability and cycling performance at high current density (Figures S13 and S14, Supporting Information). It's worth noting that the high CE of >100% points to an instability of SEI formed in glyme-based electrolyte and the instrumental error for the long-term cycling (Figures S13c,d and S14a, Supporting Information), which was commonly observed also in other previous reports.^[41,42] To better identify the most promising system, the specific gravimetric energy based on the active electrode materials, i.e., including the cathode and the stoichiometric mass of sodium, but not including the masses of Super C65, binder and current collector, was calculated from the discharge voltage profiles (Figure 6e and Figure S15, Supporting Information). A maximum value of ≈180 and 130 W h kg⁻¹ at 0.12 A g⁻¹ for Cu_{2-x}Se@C||NVP/C and Cu_{1.8}S@C||NVP/C and 316 and 284 W h kg⁻¹ for Na||Cu_{1.8}S@C and Na||Cu_{2-x}Se@C cells at 0.1 A g⁻¹, respectively. These results indicate that the copper chalcogenides are more promising as positive electrode material in sodium-metal cells rather than as negative electrode material in SIBs.

3. Conclusions

In summary, two copper chalcogenides-carbon composites (Cu_{1.8}S@C and Cu_{2-x}Se@C) have been successfully synthesized by a facile MOF-derived sulfidation/selenidation strategy. These materials show excellent sodium storage capacity and long-term cycling stability. The electrode materials display capacity retention of 90.6% after 450 cycles for Cu_{1.8}S@C and 88.1% after 1200 cycles (@ 2 A g⁻¹) for Cu_{2-x}Se@C. Given the wide operative voltage window, such composites can be used both as anodes and cathode materials. The Cu_{2-x}Se@C||NVP/C full cell revealed an excellent rate performance and a highly stable cycling performance with negligible capacity fading after 500 cycles. When used as the cathodes in Na metal cells (with limited discharge cut-off), both Na||Cu_{2-x}Se@C and Na||Cu_{1.8}S@C cells exhibits excellent power capability and cycling stability. According to the specific energy density values estimated for each system, it is evident that copper chalcogenides are promising for use as cathode material.

3. Experimental Section

Chemicals: Sulfur powder (S, 99.98%) and Cu(NO₃)₂·3H₂O (98.0–103%) were obtained from Sigma-Aldrich. Selenium powder (Se, ≥99.5%) was purchased from Alfa Aesar. 1,3,5-benzenetricarboxylic acid (BTC, 98%) was obtained from Acros Organics. Methanol (98.5%) was purchased from VWR. Polyvinylpyrrolidone (PVP, K30, Mw = 44 000–54 000) was obtained from PanReac AppliChem. All the chemicals were directly used as received without further purification.

Synthesis of Cu-BTC Precursors: The Cu-BTC precursors were synthesized via a simple solution-based method. Typically, 0.9 g Cu(NO₃)₂·3H₂O and 0.4 g polyvinylpyrrolidone (PVP, K-30) were dissolved in 50 mL of methanol under vigorous stirring. 1,3,5-Benzenetricarboxylic acid (BTC, 0.43 g) were dispersed into an additional 50 mL batch of methanol under vigorous stirring and slowly injected into the former solution. After complete mixing, the mixture was aged at room temperature for 24 h. The precipitate (Cu-BTC) was collected via

centrifugation and washed with methanol several times. Finally, it was dried at 80 °C overnight to obtain the precursor powder.

Synthesis of Na-Storage Materials: The composites were obtained by a one-step sulfidation/selenidation process. Cu-BTC and sulfur powders (in a mass ratio of 1:5) were put downstream and upstream, respectively, in the same crucible in a tube furnace under argon flow. The furnace was heated at a rate of 2 °C min⁻¹ up to 500 °C and then for 2 h. After cooling down to room temperature, Cu_{1.8}S@C was obtained. The Cu_{2-x}Se@C material was synthesized via the same procedure and same mass ratio by replacing sulfur powder with selenium powder.

Synthesis of Carbon-Coated Na₃V₂(PO₄)₃ Composite Cathode Material: The carbon-coated Na₃V₂(PO₄)₃ (NVP/C) composite was synthesized by a simple sol-gel method. Typically, CH₃COONa·3H₂O (VWR, ≥99%), NH₄H₂PO₄ (Alfa Aesar, ≥99%), NH₄VO₃ (Sigma-Aldrich, ≥99%), and citric acid monohydrate (C₆H₈O₇·H₂O) (Alfa Aesar, ≥99%) were dissolved in deionized water and dried at 80 °C. The obtained powder was ground, preheated at 350 °C for 6 h, and annealed at 800 °C for 12 h in a tube furnace under Argon flow. After natural cooling down to room temperature, the Na₃V₂(PO₄)₃/C composite was collected.

Materials Characterization: The powder XRD patterns were recorded on a Bruker D8 Advance diffractometer employing the Cu-k_α radiation (λ = 0.154 nm). In situ XRD analysis of Cu_{1.8}S@C and Cu_{2-x}Se@C was performed with a home-made cell (Be window as the current collector) with the potential controlled by a potentiostat/galvanostat (SP-150, Biologic). The morphological characteristics and elemental compositions were examined via SEM (SEM, ZEISS 1550VP) coupled with an energy dispersion X-ray spectroscopy (EDX, Oxford). TEM was performed on a ThermoFisher Talos 200X. The Raman spectra of all samples were carried out on a confocal InVia Raman microspectrometer (He-Ne laser of 633 nm, Renishaw). TGA was performed at a heating rate of 5 °C min⁻¹ (TGA-209F, Netzsch) under an oxygen flow (20 cc min⁻¹). The pore size distribution and specific surface area of all samples were carried out at 87 K via Ar physisorption (Autosorb-iQ, 3P instruments). XPS measurements of Cu_{1.8}S@C and Cu_{2-x}Se@C were performed in an ultrahigh vacuum analysis system (10⁻¹⁰ mbar) by using monochromatic Al Kα (1486.6 eV) X-ray radiation and Phoibos 150 XPS spectrometer (SPES- Surface concept) equipped with a microchannel plate and a delay line detector in fixed transition mode. The high-resolution spectra were acquired at 400 W, 20 eV pass energy and 0.1 eV energy step. The peak fitting was analyzed by CasaXPS software, and adventitious carbon (C-C/C-H) peak at 285 eV was used as calibration. Shirley background and a 70% Gaussian and 30% Lorentzian (GL30) profile function were used, except for C-C/C-H (asymmetric line-shape).

Electrochemical Measurements: The working electrodes were fabricated by casting slurries containing either Cu_{1.8}S@C or Cu_{2-x}Se@C, and Super C65 (Imerys Graphite & Carbon), and polyvinylidene fluoride (Solef 6020, Solvay) in N-methyl pyrrolidone (NMP, anhydrous, Sigma-Aldrich) in a weight ratio of 70:20:10 onto a dendritic copper foil (Schlenk, 99.9%). The coated films were dried in an oven at 80 °C for 2 h in air. Punched disk electrodes (12 mm in diameter) were further vacuum-dried for 24 h at 80 °C. The active material mass loading of the electrodes ranged between 1.2 and 1.5 mg cm⁻². The NVP/C cathode electrodes were made by casting a slurry composed of NVP/C, Super C65 (Imerys Graphite & Carbon), and polyvinylidene fluoride (Solef 6020, Solvay) (weight ratio of 80:10:10) dispersed in N-methyl pyrrolidone, onto aluminum foil. After drying for 2 h at 80 °C in air, 12 mm diameter disk were punched and further vacuum-dried for 24 h at 120 °C. Before cell assembly, all the electrodes were pressed at 5 tons cm⁻² for 10 s to increase their density. All cells were assembled in an argon-filled glovebox (MBraun) with H₂O and O₂ content < 0.1 ppm.

Galvanostatic cycling tests were carried out in CR2032 coin cells, using Cu_{1.8}S@C or Cu_{2-x}Se@C as working electrode, sodium metal foil (Acros, 99.5%) as counter electrode, 1 M NaPF₆ solution in DEGDM as electrolyte, and a glass fiber membrane disk (GF/D, Whatman) as the separator. For the Cu_{1.8}S@C or Cu_{2-x}Se@C||NVP/C full cell measurement, the Cu_{1.8}S@C or Cu_{2-x}Se electrode was presodiated (10 cycles at 0.1 A g⁻¹) to offset the initial irreversible capacity. The capacity ratio of the anode and cathode (n/p) in full cell ranged from

1.35 to 1.5, i.e., all cells were cathode limited. Cyclic voltammeteries (CV) were performed in three-electrode Swagelok T-type cells with a VMP3 potentiostat in the voltage range of 0.01–2.5 V or 0.5–3.0 V versus Na/Na⁺. The galvanostatic cycling tests were performed on a Maccor 3000 battery tester. All measurements were performed at a constant temperature of 20 ± 1 °C.

Supporting Information

Supporting Information is available from the Wiley Online Library or from the author.

Acknowledgements

The authors thank Seyed Milad Hosseini for the Raman measurement and Hyein Moon for the BET measurement. The authors also thank Dr. Zhen Chen and Dr. Fanglin Wu for valuable discussions. H.L. gratefully acknowledged financial support from the Chinese Scholarship Council (CSC). Financial support from the Helmholtz Association and the German Ministry for Education and Research (BMBF, within the M.Era-net project “NEILLSBAT,” 03XP0120A) was also acknowledged. This work contributed to the research performed at CELEST (Center for Electrochemical Energy Storage Ulm-Karlsruhe).

Open access funding enabled and organized by Projekt DEAL.

Conflict of Interest

The authors declare no conflict of interest.

Authors Contributions

H.L. conceived the research idea, designed the experiments, analyzed the results, and prepared the first draft of the manuscript. H.Z. provided some research ideas and cathode materials. M.Z. contributed to the characterization by XPS. H.-P.L. contributed to the full cell measurement. D.G. and U.K. contributed to the characterization by TEM. A.V. and S.P. supervised, coordinated the work, and provided funding. All authors contributed to the writing and have given approval to the final version of the manuscript.

Data Availability Statement

The data that support the findings of this study are available on request from the corresponding author. The data are not publicly available due to privacy or ethical restrictions.

Keywords

copper composite, copper chalcogenides, metal-organic frameworks, Na-ion storage, sodium batteries

Received: March 17, 2022
Published online: April 27, 2022

- [1] M. Li, J. Lu, Z. Chen, K. Amine, *Adv. Mater.* **2018**, *30*, 1800561.
[2] L. Lu, X. Han, J. Li, J. Hua, M. Ouyang, *J. Power Sources* **2013**, *226*, 272.
[3] N. Yabuuchi, K. Kubota, M. Dahbi, S. Komaba, *Chem. Rev.* **2014**, *114*, 11636.
[4] J. Y. Hwang, S. T. Myung, Y. K. Sun, *Chem. Soc. Rev.* **2017**, *46*, 3529.

- [5] H. Zhang, B. Qin, J. Han, S. Passerini, *ACS Energy Lett.* **2018**, *3*, 1769.
[6] H. Zhang, I. Hasa, B. Qin, T. Diemant, D. Buchholz, R. J. Behm, S. Passerini, *ChemElectroChem* **2017**, *4*, 1256.
[7] H. Zhang, S. Jeong, B. Qin, D. V. Carvalho, D. Buchholz, S. Passerini, *ChemSusChem* **2018**, *11*, 1382.
[8] W. Chen, X. Zhang, L. Mi, C. Liu, J. Zhang, S. Cui, X. Feng, Y. Cao, C. Shen, *Adv. Mater.* **2019**, *31*, 1806664.
[9] D. Bresser, S. Passerini, B. Scrosati, *Energy Environ. Sci.* **2016**, *9*, 3348.
[10] Y. Xiao, Y. F. Zhu, H. R. Yao, P. F. Wang, X. D. Zhang, H. Li, X. Yang, L. Gu, Y. C. Li, T. Wang, Y. X. Yin, X. D. Guo, B. H. Zhong, Y. G. Guo, *Adv. Energy Mater.* **2019**, *9*, 1803978.
[11] S. Guo, Q. Li, P. Liu, M. Chen, H. Zhou, *Nat. Commun.* **2017**, *8*, 135.
[12] H. Tan, Y. Feng, X. Rui, Y. Yu, S. Huang, *Small Methods* **2019**, *4*, 1900563.
[13] G. Fang, Q. Wang, J. Zhou, Y. Lei, Z. Chen, Z. Wang, A. Pan, S. Liang, *ACS Nano* **2019**, *13*, 5635.
[14] H. Li, Y. Ma, H. Zhang, T. Diemant, R. J. Behm, A. Varzi, S. Passerini, *Small Methods* **2020**, *4*, 2000637.
[15] Y. Fang, X. Y. Yu, X. W. D. Lou, *Angew. Chem., Int. Ed.* **2019**, *58*, 7744.
[16] H. Lin, M. Li, X. Yang, D. Yu, Y. Zeng, C. Wang, G. Chen, F. Du, *Adv. Energy Mater.* **2019**, *9*, 1900323.
[17] D. Chen, G. Chen, R. Jin, H. Xu, *CrystEngComm* **2014**, *16*, 2810.
[18] S. L. James, *Chem. Soc. Rev.* **2003**, *32*, 276.
[19] J. L. Rowsell, O. M. Yaghi, *Angew. Chem., Int. Ed.* **2005**, *44*, 4670.
[20] R. J. Kuppler, D. J. Timmons, Q.-R. Fang, J.-R. Li, T. A. Makal, M. D. Young, D. Yuan, D. Zhao, W. Zhuang, H.-C. Zhou, *Coord. Chem. Rev.* **2009**, *253*, 3042.
[21] L. E. Kreno, K. Leong, O. K. Farha, M. Allendorf, R. P. Van Duyne, J. T. Hupp, *Chem. Rev.* **2012**, *112*, 1105.
[22] X. Xu, R. Cao, S. Jeong, J. Cho, *Nano Lett.* **2012**, *12*, 4988.
[23] J. Rong, J. Xu, F. Qiu, Y. Zhu, Y. Fang, J. Xu, T. Zhang, *Adv. Mater. Interfaces* **2019**, *6*, 1900502.
[24] X. Xu, J. Liu, J. Liu, L. Ouyang, R. Hu, H. Wang, L. Yang, M. Zhu, *Adv. Funct. Mater.* **2018**, *28*, 1707573.
[25] P. Wang, M. Shen, H. Zhou, C. Meng, A. Yuan, *Small* **2019**, *15*, 1903522.
[26] Q. Liu, S. Zhang, Y. Xu, *Nanomaterials* **2020**, *10*, 1034.
[27] S. Foley, H. Geaney, G. Bree, K. Stokes, S. Connolly, M. J. Zaworotko, K. M. Ryan, *Adv. Funct. Mater.* **2018**, *28*, 1800587.
[28] J. Xiao, H. Liu, J. Huang, Y. Lu, L. Zhang, *Appl. Surf. Sci.* **2020**, *526*, 146746.
[29] H. Li, H. Zhang, T. Diemant, R. Jürgen Behm, D. Geiger, U. Kaiser, A. Varzi, S. Passerini, *Small Structures* **2021**, *2*, 2100035.
[30] M. C. Biesinger, L. W. M. Lau, A. R. Gerson, R. S. C. Smart, *Appl. Surf. Sci.* **2010**, *257*, 887.
[31] A. J. C. D. Wagner, *J. Electron Spectrosc. Relat. Phenom.* **1988**, *47*, 283.
[32] M. C. Biesinger, *Surf. Interface Anal.* **2017**, *49*, 1325.
[33] D. Chen, Y. Zhang, X. Li, J. Shen, Z. Chen, S.-a. Cao, T. Li, F. Xu, *Chem. Eng. J.* **2020**, *384*, 123235.
[34] Y. Li, X. Sun, Z. Cheng, X. Xu, J. Pan, X. Yang, F. Tian, Y. Li, J. Yang, Y. Qian, *Energy Storage Mater.* **2019**, *22*, 275.
[35] Y. Liu, S. Shen, J. Zhang, W. Zhong, X. Huang, *Appl. Surf. Sci.* **2019**, *478*, 762.
[36] Y. Ma, Y. Ma, G. T. Kim, T. Diemant, R. J. Behm, D. Geiger, U. Kaiser, A. Varzi, S. Passerini, *Adv. Energy Mater.* **2019**, *9*, 1902077.
[37] V. V. Singh, A. K. Singh, *Dalton Trans.* **2015**, *44*, 725.
[38] F. Li, T. Li, C. Sun, J. Xia, Y. Jiao, H. Xu, *Angew. Chem., Int. Ed.* **2017**, *56*, 9910.
[39] C. H. Choi, M. W. Chung, Y. J. Jun, S. I. Woo, *RSC Adv.* **2013**, *3*, 12417.
[40] L. Hu, C. Shang, E. M. Akinoglu, X. Wang, G. Zhou, *Nanomaterials* **2020**, *10*, 302.
[41] T. Liu, Y. Li, L. Zhao, F. Zheng, Y. Guo, Y. Li, Q. Pan, Y. Liu, J. Hu, C. Yang, *ACS Appl. Mater. Interfaces* **2019**, *11*, 19040.
[42] D. Yang, W. Chen, X. Zhang, L. Mi, C. Liu, L. Chen, X. Guan, Y. Cao, C. Shen, *J. Mater. Chem. A* **2019**, *7*, 19709.